Geophysical Research Letter

Supporting Information for

Continuous dissolved gas tracing of fracture-matrix exchanges

R. Hoffmann[1,2,†], P. Goderniaux[2], P. Jamin[1], E. Chatton[3], J. de la Bernardie[3], T. Labasque[3], T. Le Borgne[3], A. Dassargues[2]

[1] Hydrogeology & Environmental Geology, UEE, Liège University, Liège, Belgium
[2] Geology and Applied Geology, Polytech Mons, University of Mons, Mons, Belgium
[3] Geoscience Rennes, University Rennes 1, Rennes, France

Corresponding author: Richard Hoffmann (Richard.Hoffmann@uliege.be)

† ITN ENIGMA received funding from European Union's Horizon 2020 research and innovation programme under the Marie Sklodowska-Curie Grant Agreement N°722028.

Contents of this file

This file contains supporting information regarding the field site and experimental set up (Text S1, Figure S1 to S4), the fracture-matrix and channel-matrix transport models (Text S2, Figure S5) and a simplified sensitivity analysis (Text S3, S4 and Figure S6-S10).

Text S1: Test site and experimental set up

The experimental test site consists in two adjacent 50 m-deep wells (Pz1 and Pz2), distant 7.55 m, drilled in the porous/fractured chalk aquifer of the Mons sedimentary Basin in South-West Belgium (Figure S1a and b). Various hydraulic and tracer experiments (Goderniaux et al., 2018), optical imaging and flowmeter tests allowed characterizing the hydraulic connectivity between Pz1 and Pz2, and fracture locations. Pumping tests give an estimated mean hydraulic conductivity of 3×10^{-5} m s^{-1}. Hydraulic experiments performed on individual 1 m long isolated sections of the boreholes provide equivalent hydraulic conductivity values between 1.9×10^{-4} m s^{-1} and 9.0×10^{-7} m s^{-1}, depending on the presence of fractures (Goderniaux et al., 2018).

Fractures mainly consist in horizontal stratigraphic joints connected by diaclases. Density of stratigraphic joints is about 3 per meter. At 34.8 m depth an open fracture is identified, which connects Pz1 and Pz2 and is isolated for this study using an inflatable double packer system (Figure S1c,d). The background groundwater temperature is around 12 °C. Before the experiments, conditions are anoxic (8.23×10^{-6} mol L^{-1} oxygen).

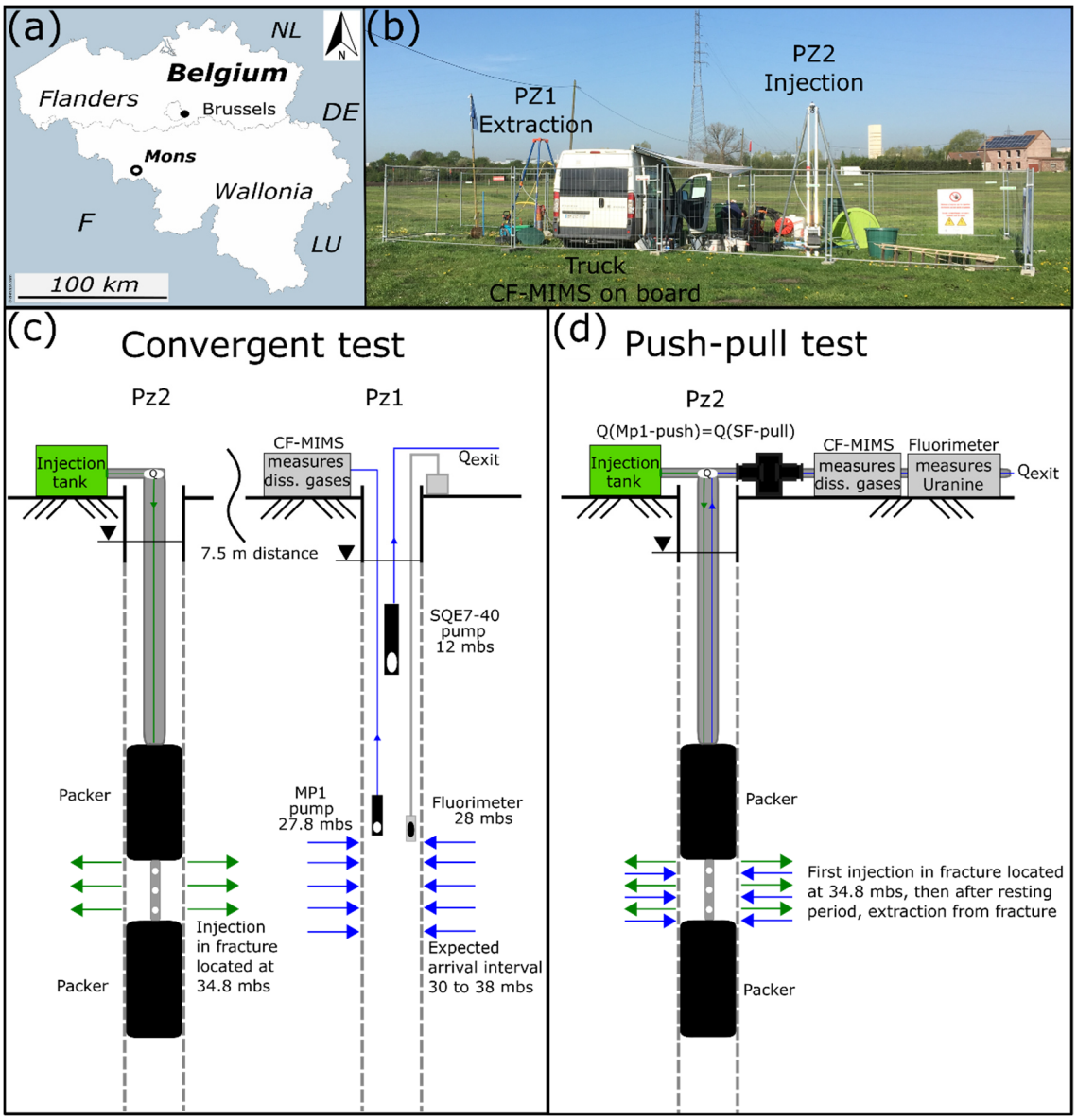

Figure S1. a) Test site location nearby Mons city, South-West Belgium, and b) field site picture. Experimental setup of the dissolved gas and solute injection tests: c) in convergent and d) in push-pull configuration (SF: Surface pump, mbs: meter below surface, MP1 and SQE7-40: names of the used submersible pumps).

In this study, a cocktail of dissolved gases (He, Ar, Xe) was injected jointly with uranine in a specific open fracture of PZ2, located 34.8 m deep, and isolated using an inflatable double packer system (Q=0.57 m^3 h^{-1}) (Figure S1c,d). Tracers were injected (1) in a convergent configuration with injection in Pz2 and recovery in Pz1 (Figure S1c), and (2) in a push-pull configuration in Pz2 (Figure S1d). Dissolved gas concentrations were measured on site using a mobile CF-MIMS (continuous flow membrane inlet mass spectrometer) system installed and powered in a truck converted in a mobile lab where moderate temperature effects on the membrane permeability can be accounted for (Figure S1b) (Chatton et al., 2017).

The CF-MIMS is modified from the HPR-40 Hidden analytical Membrane Inlet Mass Spectrometer and uses a large permeable membrane to continuously extract a fraction of the dissolved gases from the water flowing in the membrane contactor. The different gases are thereafter ionized by electron impacts and directed under vacuum towards the detectors by the electromagnetic field of a quadrupole mass filter which separates the ions according to their

mass-to-charge ratio (m/z). Finally, the detectors (Faraday cup or electron multiplier) record the signal produced by each m/z which can be related to the concentration of the gases dissolved in the water flow. With the CF-MIMS, dissolved gas tracers can be measured simultaneously in the field at high-frequency (1 measurement every 2 seconds) over a large range of concentrations.

In the convergent experiment, the forced gradient was generated using a pump (3 inches SQE7-40) installed in PZ1 on top of the water column (Q=7.2 m^3 h^{-1}). Uranine concentrations were measured using a field fluorimeter installed at 28 m deep, just above the tracer arrival zone located between 30 and 38 m deep (Goderniaux et al., 2018). At 27.8 m (same depth), an additional sampling pump (2 inches MP1) was continuously conveying water from the tracer arrival zone to the CF-MIMS with a flow rate of 0.24 m^3 h^{-1}, for continuous analysis of the dissolved gases concentrations (Figure S1c). The corresponding raw concentrations related to the background concentrations measured before the convergent test (natural condition) are shown in Figure S2.

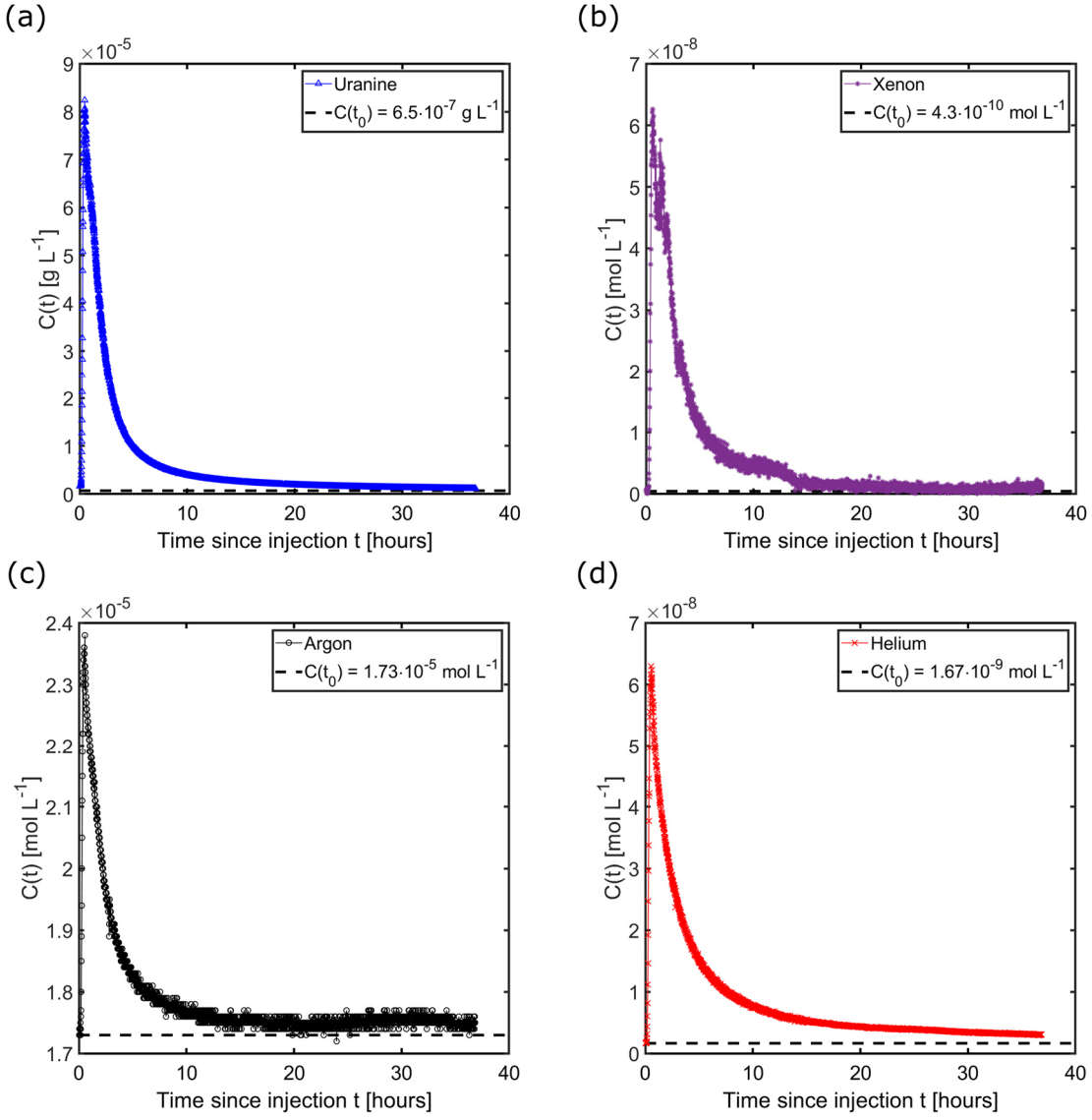

Figure S2: Raw concentrations measured during the convergent test in PZ1 for (a) uranine, (b) xenon, (c) argon and (d) helium, visualized in linear scales.

In the push-pull experiment, no pumping was performed in PZ1. Recovery was implemented using a surface pump. Injection and extraction flow rate were each time Q=0.57 m^3 h^{-1}. The CF-MIMS and a surface fluorimeter were installed in series along the recovery pipes, at the level of the ground surface (Figure S1d). The corresponding raw concentrations related to the background concentrations measured before the convergent test (natural condition) are shown in Figure S3. During both experiments, the monitoring CF-MIMS of dissolved gases was verified by additional gas-chromatographic measurements on samples.

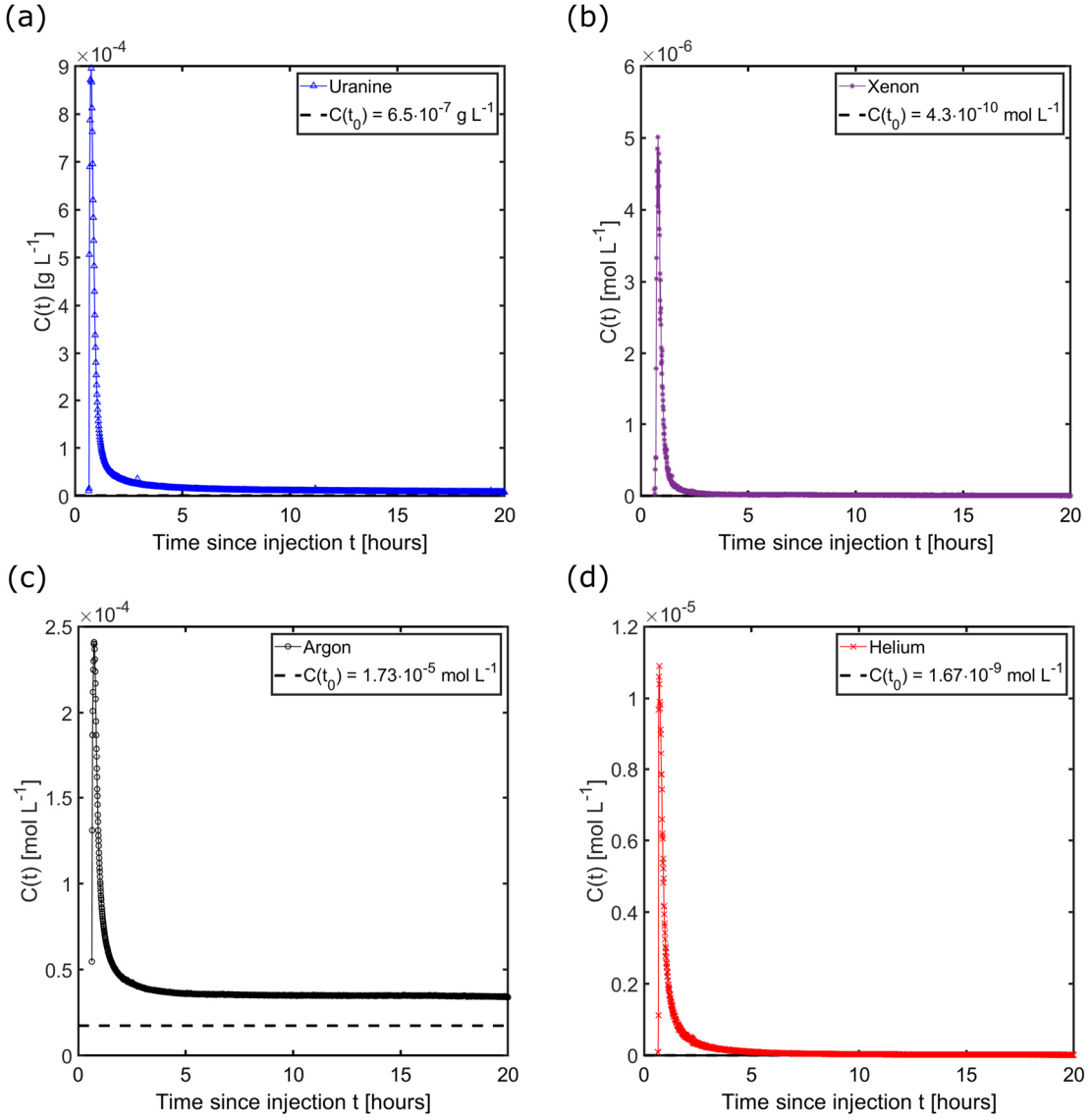

Figure S3: Raw concentrations measured during the push-pull test in PZ2 for (a) uranine, (b) xenon, (c) argon and (d) helium, visualized in linear scales.

In Figure S4, the raw concentrations are visualized in log-log scales, with an indication of the background concentrations before the convergent experiment (natural condition) (Figure S4a and b) and the detection limit of the CF-MIMS system (Figure S4c and d).

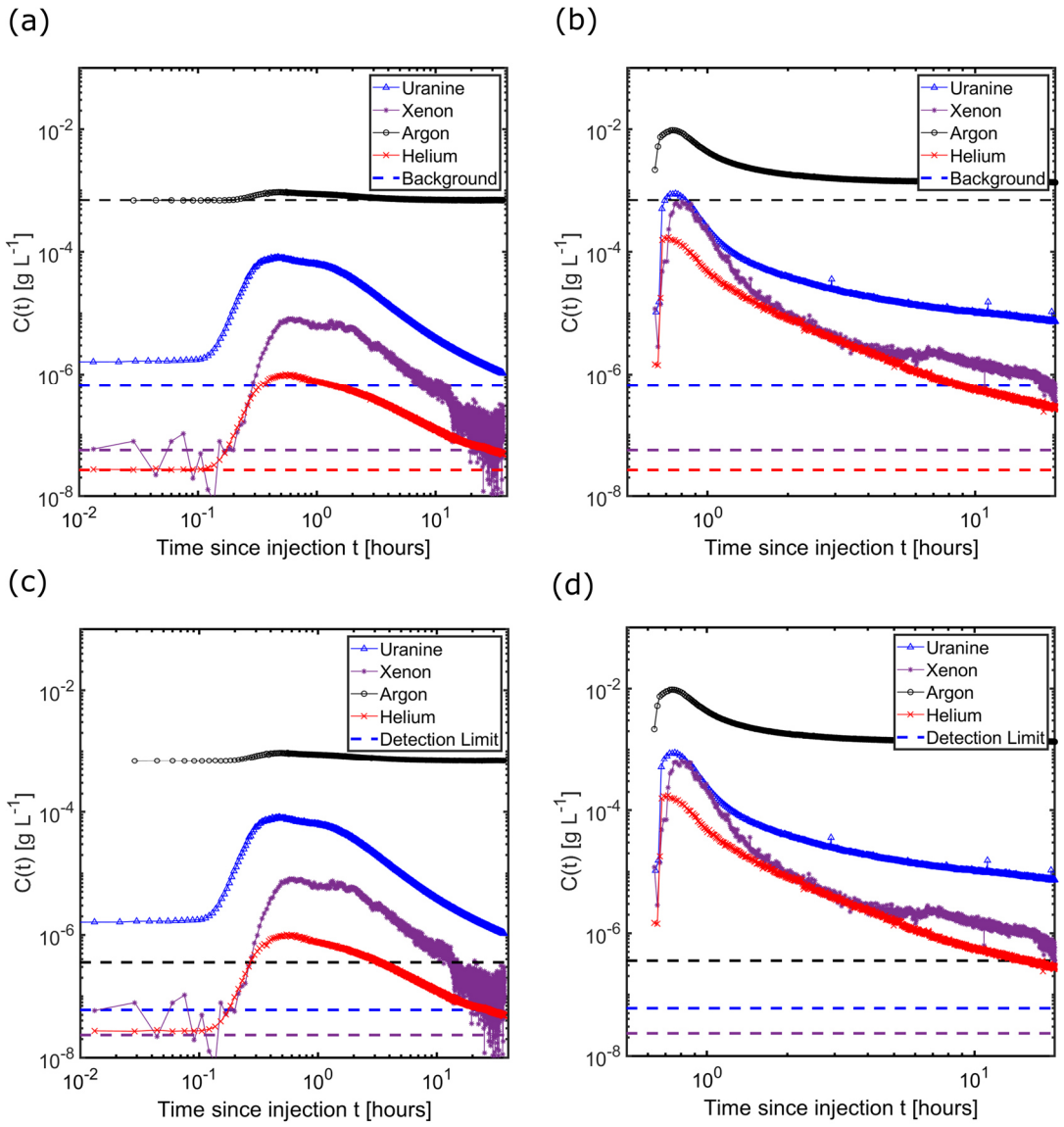

Figure S4: Raw concentrations measured during the convergent (a and c) and push-pull (b and d) tests, visualized in log-log scales. Background and detection limits are provided in graphs (a) and (b) and graphs (c) and (d), respectively. Note, the detection limit of helium is 7×10^{-12} g L^{-1} and not shown for readability.

Text S2: Analytical model for fracture-matrix transport

1. Model definition

The models consider a series of parallel fractures connecting wells represented as parallel plates (Figure S5a) or channels (Figure 5b). The latter geometry represents highly channelized flow in fractures, which plays an important role in matrix diffusion processes (Klepikova et al. 2016).

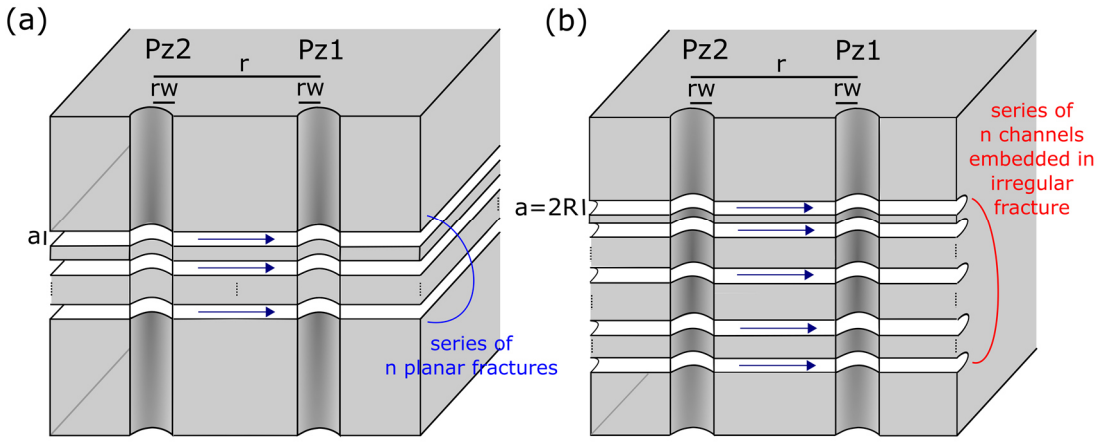

Figure S5. Schematic visualization of the considered fracture geometries. Flow and transport between the two wells is conceptualized by (a) a series of multiple planar fractures and (b) multiple channels, embedded in irregular fracture planes (see also Figure 2 in the manuscript for the visualization of the concept of the channels).

Assuming that solute diffusion occurs mainly in the direction perpendicular to the fracture-matrix interface, transport in the fracture and the matrix is described by (Carrera et al., 1998, Klepikova et al. 2016, De la Bernardie et al. 2018, 2019):

$$\frac{\partial c_f}{\partial t} = -u\nabla c_f + \nabla(D\nabla c_f) - F_m \quad (1)$$

$$F_m = \sigma_m(\eta = 0)D_m \frac{\partial c_m}{\partial \eta}\Big|_{\eta=0} \quad (2)$$

and

$$\sigma_m(\eta)\frac{\partial c_m}{\partial t} = \frac{\partial}{\partial \eta}\left(\sigma_m(\eta)D_m\frac{\partial c_m}{\partial \eta}\right) \quad (3)$$

where c_f and c_m are respectively the fracture and matrix tracer concentrations, u is the flow velocity in the fracture, F_m is the diffusive flux from the fracture to the matrix, η is the depth into the matrix measured from the fracture wall, D_m is the tracer molecular diffusion in the matrix, $D = \alpha u$ is the longitudinal dispersion coefficient with α as the dispersivity and σ_m is the specific surface area of matrix that accounts for the matrix geometry (m^{-1}) as planar fracture (4) and channel (5), respectively:

$\sigma_m(\eta) = 2/a$, for planar fractures (Figure S5a) (4)

$\sigma_m(\eta) = 2(a + \eta)/a^2$, for channels (Figure S5b) (5)

Initial and boundary conditions of equation (1) and (3) are:

$$c_m(x, \eta, t = 0) = c_f(x, t = 0) = 0 \quad (6)$$

$$c_f(x = 0, t) = S(t) \quad (7)$$

$$c_m(x, \eta = 0, t) = c_f(x, t) \tag{8}$$

$$\frac{\partial c_m}{\partial \eta}(x, \eta = \infty, t) = 0 \tag{9}$$

where x is the coordinate along the fracture and $S(t)$ is a source term describing the tracer injection.

Equations (1) to (3), subjected to the boundary conditions (6) to (9) can be solved by expressing the matrix concentration as a convolution of the fracture concentration (Carrera et al., 1998, Klepikova et al. 2016, De la Bernardie et al. 2018, 2019):

$$c_m(x, \eta, t) = \int_0^t dt' \, G(\eta, t - t') c_f(x, t') = \; G * c_f \tag{10}$$

where $G(\eta, t)$ is the Green's function (s^{-1}), which solves (3) for the boundary condition $G(\eta = 0, t) = \delta(t)$. Integrating equation (3) in space, one obtains the diffusive flux from the fracture to the matrix,

$$F_m = \frac{\partial}{\partial t} \int_0^\infty d\eta \, \sigma_m(\eta) \, c_m(x, \eta, t) = \frac{\partial}{\partial t} \int_0^t dt' \int_0^\infty d\eta \, \sigma_m(\eta) G(\eta, t - t') c_f(x, t') \tag{11}$$

Defining φ as the memory function (s^{-1}):

$$\varphi(t) = \int_0^\infty d\eta \, \sigma_m(\eta) G(\eta, t) \tag{12}$$

This gives:

$$F_m = \frac{\partial}{\partial t}(\varphi * c_f) = \varphi * \frac{\partial}{\partial t} c_f \tag{13}$$

Inserting (13) in (1), the Laplace transform of (1) leads to (Barker, 2010; Carrera et al., 1998, De la Bernardie et al. 2018, 2019):

$$-u \cdot \nabla \bar{c}_f + \nabla(D \nabla \bar{c}_f) + p(1 + \bar{\varphi}) \bar{c}_f = 0 \tag{14}$$

where the overbar expresses Laplace transformation, and p is the Laplace variable. The solution of equation (14) for a Dirac source $S(t) = \Delta c_i \Delta t_i \delta(t)$ depends on the flow geometry (among others, linear flow, dipole flow, convergent flow, push-pull) and on the specific surface area of matrix $\sigma_m(\eta)$ that accounts for the matrix geometry (m^{-1}) (equations (4) and (5)).

2. Solution for planar fracture flow in cross borehole test

For a convergent radial flow in planar fractures (Figure S5a), the solution of equation (14) is (Becker and Charbonneau, 2000),

$$\bar{c}_f(p) = \Delta c_i \Delta t_i \exp\left(\frac{r - r_w}{2\alpha}\right) \frac{\mathrm{Ai}\left(\left(\frac{2s\alpha^2}{r^2 - r_w^2}\right)^{-\frac{2}{3}} \left(r \frac{2s\alpha}{r^2 - r_w^2} + \frac{1}{4}\right)\right)}{\mathrm{Ai}\left(\left(\frac{2s\alpha^2}{r^2 - r_w^2}\right)^{-\frac{2}{3}} \left(r_w \frac{2s\alpha}{r^2 - r_w^2} + \frac{1}{4}\right)\right)} \tag{15}$$

with r the distance between the injection point and the pumping well, r_w the pumping well radius and,

$$s = \tau_a p(1 + \sigma \bar{\varphi}) \tag{16}$$

where $\tau_a = n_f \pi r^2 a/Q$ is the characteristic advection time from the injection point to the pumping well, with Q the pumping rate and n_f the number of fractures. For diffusion in the direction perpendicular to the planar fracture, the memory function is (De la Bernardie et al. 2019),

$$\bar{\varphi} = \frac{1}{\sqrt{p\tau_D}} \tag{17}$$

with $\tau_D = a^2/D_m$ as the diffusion time over the fracture aperture a.

3. Solution for channel fracture flow in cross borehole test

For flow in channels of length L and diameter a joining the injection and observation points (Figure S5b), the solution of equation (14) is (De la Bernardie et al. 2018),

$$\bar{c}_f(p) = \Delta c_i \Delta t_i e^{\frac{L}{2\alpha}\left(1-\sqrt{1+4pt_a\frac{\alpha}{L}(1+\sigma\bar{\varphi})}\right)} \tag{18}$$

where $\tau_a = n_c r\pi a^2/4Q_c = n_c r\pi R^2/Q_c$ is the advective transit time in the channel, R the channel radius (a=2R) and $Q_c = f\,Q$ where f is the fraction of the pumping flow rate participating to tracer transport. Here f is estimated as the ratio of the injected and measured maximum concentration, $f \approx 3 \times 10^{-3}$ for the convergent experiment.

For radial diffusion in the direction perpendicular to the channels, the memory function is (De la Bernardie et al. 2019),

$$\bar{\varphi} = \frac{2}{\sqrt{p\tau_D}} \frac{K_1\left(\sqrt{p\tau_D}\right)}{K_0\left(\sqrt{p\tau_D}\right)} \tag{19}$$

with $\tau_D = a^2/D_m$ and $K_{i=0,1}$ are the modified Bessel functions of the second kind.

4. Solution for planar fracture flow in push-pull single borehole test

For interpreting the push-pull tracer test, the solution of transport in a divergent flow in a fracture with that of transport in a convergent flow are combined (Becker and Shapiro, 2003).

The solution of equation (14) for divergent radial flow in a fracture is (Chen et al. 2007),

$$\bar{c}_{push}(r,p) = \frac{\Delta c_i \Delta t_i \exp\left(\frac{r-r_w}{2\alpha}\right) \mathrm{Ai}\left(\left(\frac{2s\alpha^2}{r^2-r_w^2}\right)^{-\frac{2}{3}}\left(r\frac{2s\alpha}{r^2-r_w^2}+\frac{1}{4}\right)\right)}{\mathrm{Ai}\left(\left(\frac{2s\alpha^2}{r^2-r_w^2}\right)^{-\frac{2}{3}}\left(r_w\frac{2s\alpha}{r^2-r_w^2}+\frac{1}{4}\right)\right) - 2s^{\frac{1}{3}}\mathrm{Ai}'\left(\left(\frac{2s\alpha^2}{r^2-r_w^2}\right)^{-\frac{2}{3}}\left(r_w\frac{2s\alpha}{r^2-r_w^2}+\frac{1}{4}\right)\right)} \tag{20}$$

with r the distance from the injection well, r_w the injection well radius, s given by equation (16) and Ai' is the first derivative of the Airy function.

In the pull phase we use (20) as an initial condition for solving with a convergent flow leading to the concentration is the pumping well and integrate over all r. Equation (20) is thus convolved with (15) and integrated over r to obtain the concentration at the well during the pull phase,

$$\bar{c}_{\text{pull}}(p) = \int_{r_w}^{\infty} dr\, \bar{c}_{\text{push}}(r,p) \exp\left(\frac{r - r_w}{2\alpha}\right) \frac{\text{Ai}\left(\left(\frac{2s\alpha^2}{r^2 - r_w^2}\right)^{-\frac{2}{3}}\left(r\frac{2s\alpha}{r^2 - r_w^2} + \frac{1}{4}\right)\right)}{\text{Ai}\left(\left(\frac{2s\alpha^2}{r^2 - r_w^2}\right)^{-\frac{2}{3}}\left(r_w\frac{2s\alpha}{r^2 - r_w^2} + \frac{1}{4}\right)\right)} \quad (21)$$

where s is given by equation (16). These equations are solved using the Laplace inversion function invlap. Analytical solutions were first validated by comparison to COMSOL simulation and then compared to field data.

Text S3: Sensitivity analysis

In order to highlight the role of model parameters, we performed a simplified sensitivity analysis by varying one parameter while keeping the other constant. Tested parameters include the number of fractures or channels, the fracture aperture or channel radius, the dispersivity and the diffusion coefficient.

For the convergent configuration, the mean travel time is controlled by the volume of fracture/channel. Hence, the peak time decreases with the number of fractures/channels (Figure S6a,b) and with their aperture (Figure S6c,d). As the travel time increases, the peak amplitude also decreases since diffusion/dispersion has more time to dilute and disperse the plume. For a fixed product of number of fractures/channels times the fracture aperture/channel radius, tailing increases with the number of fractures/channels as the surface area available for diffusive mass transfer between the fracture and the matrix increases (Figure S6e,f). Dispersivity controls the width of the breakthrough curve around the peak.

For the push-pull configuration, the mean travel time is not controlled directly by the volume of fracture as there is no advective travel time from one point to the other. However, the peak time and amplitude is sensitive to matrix diffusion. Increasing the number of fractures leads to a larger diffusive flux towards the matrix and therefore a delayed peak (Figure S7a,b). Decreasing fracture aperture leads to a faster diffusive mass transfer favoring tracer storage in the matrix close to the injection point. When flow is reversed, this mass returns to the pumping zone faster than for larger apertures and therefore the peak time is smaller (Figure S7c,d). A similar effect was observed by Klepikova et al. (2016) for heat transport.

To evaluate the benefit of using tracers with different diffusion coefficients, the sensitivity to model parameters of the curves representing peak time and amplitude as a function of diffusion coefficients was explored (Figure S8 and S9). Increasing the number of fractures/channels induces longer peak times and lower peak concentrations (Figure S8), which is consistent with the information derived from Figure S6. The dependency of peak time and amplitude to diffusion coefficient is different for the fracture and channel model, hence providing constraints on the relevant conceptual model. This highlights the interest of using tracers of different coefficients to investigate fracture-matrix interactions. Push-pull breakthrough curves are also sensitive to the number of fractures, although to a lesser extent. Both convergent and push-pull peak time and amplitude where found to be sensitive to dispersivity (Figure S9). Increasing dispersivity leads to broader residence time distributions with more diluted and delayed peak. Note that the best fit parameters for the channel model leads to a smaller dispersivity than for the parallel plate model. This is probably due to the different distribution of velocities in the two models. The dispersion coefficient is the product of the local velocity and the dispersivity. In the parallel plate model, the velocity is small at the injection point and accelerates strongly close to the pumping well. Because velocity is small over a large part of streamlines, a larger dispersivity is needed in the parallel plate model to achieve a similar dispersion as in the channel model, where the velocity is constant along streamlines.

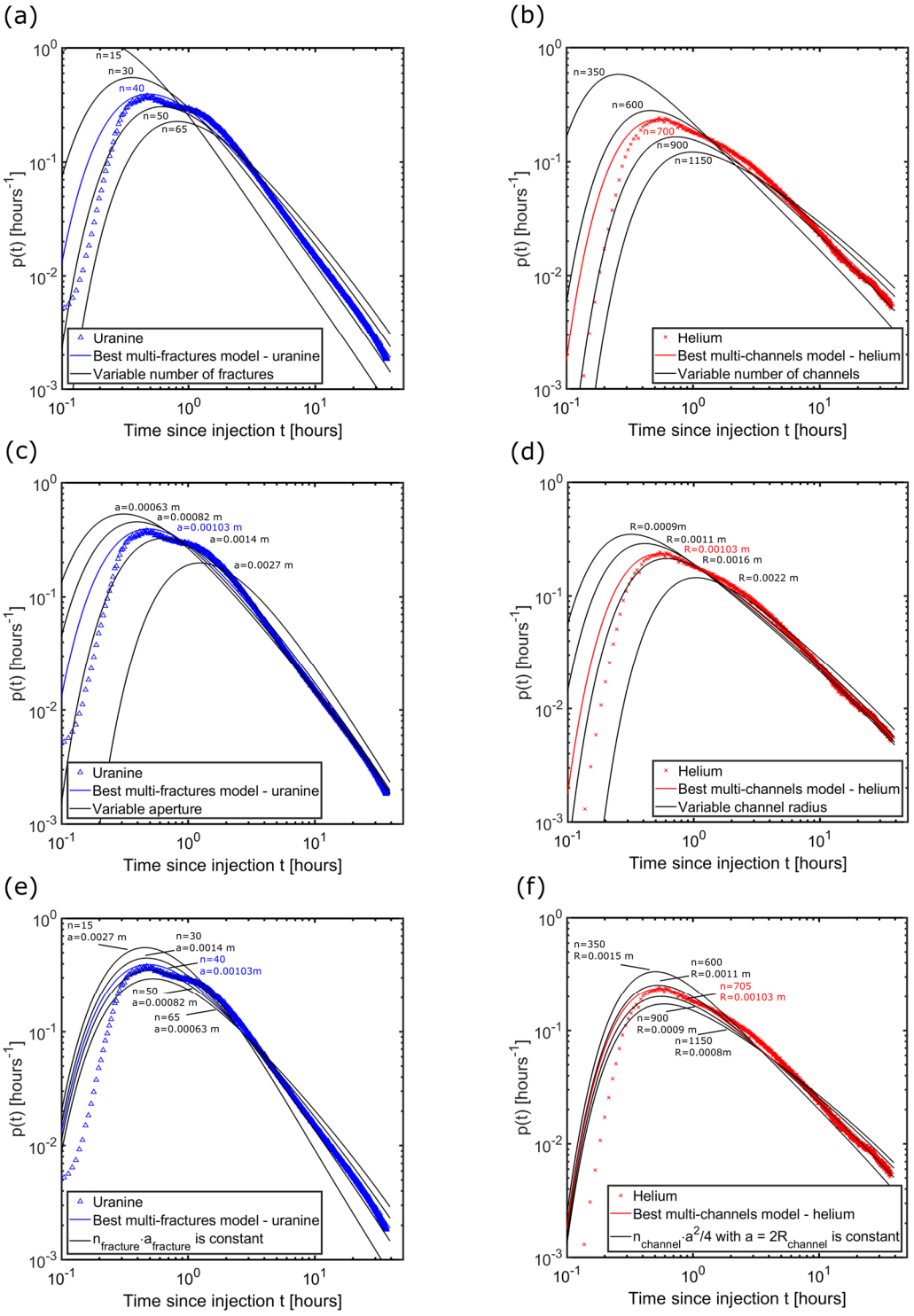

Figure S6. Sensitivity analysis of modelled breakthrough curves to the fracture/channel aperture/radius and number for the convergent configuration. For the fracture model, results are compared to the uranine breakthrough curve. We varied the number of fractures from n_f =15 to n_f =65 (a), the aperture from a=6.3 10^{-4} m to a=2.7 10^{-3} m (c) and the number of fractures from n_f=15 to n_f =65 while varying the aperture to keep the product n_f×a constant (e). For the channel model, results are compared to the helium breakthrough curve. We varied the number of channels from n_c =350 to n_c =1150 (b), the radius from R=9 10^{-4} m to R=2.2 10^{-3} m (d) and the number of channels from n_c =350 to n_c =1150 while varying the radius to keep the product n_c×R constant (f).

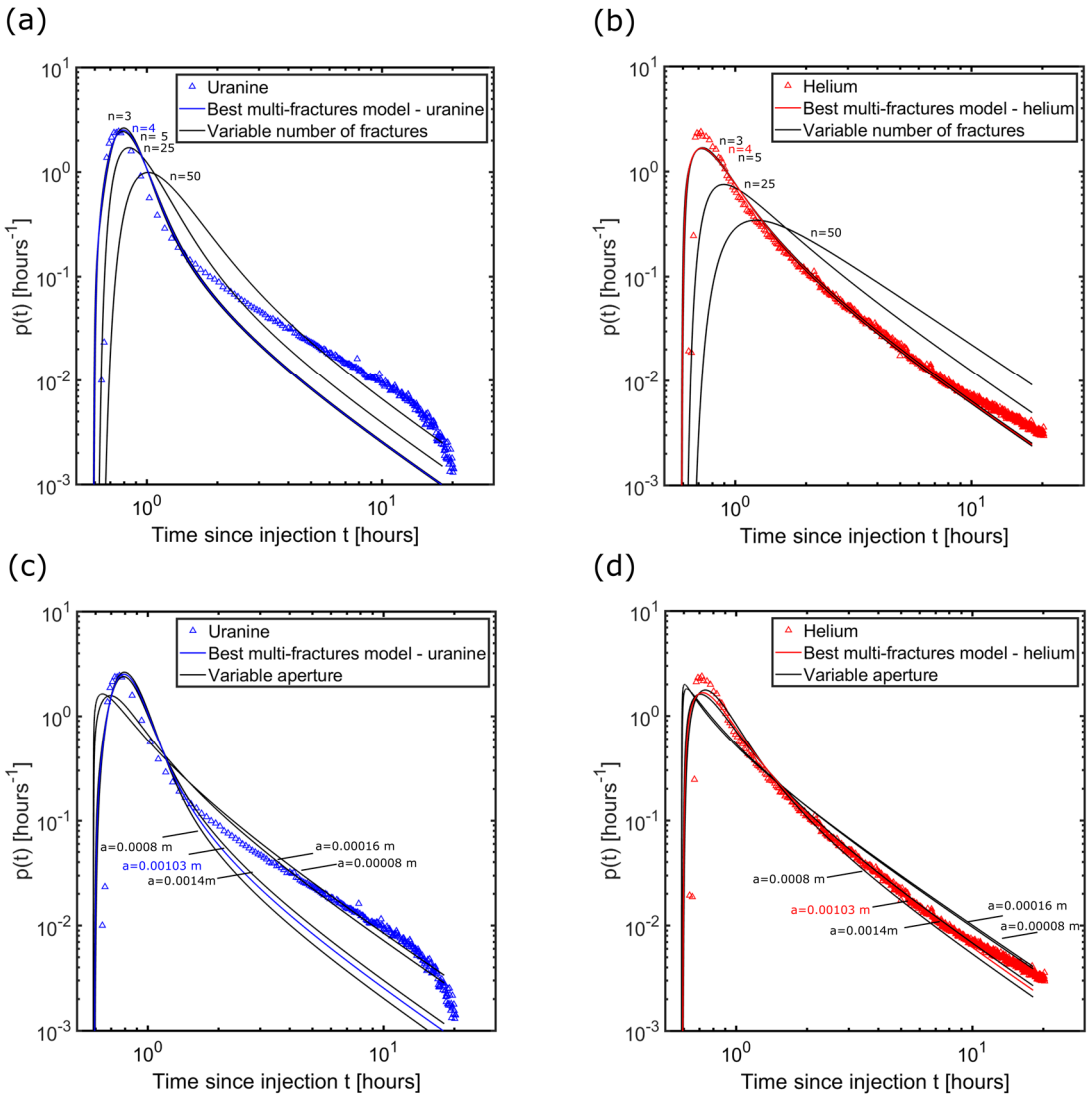

Figure S7. Sensitivity analysis of modelled breakthrough curves to the fracture aperture and number for the push-pull configuration and the fracture model. For the uranine breakthrough curve, we varied the number of fractures from n=3 to n=50 (a), and the aperture from a=8 10^{-4} m to a=1.4 10^{-3} m (c). For the helium breakthrough curve, we varied the number of fractures from n=3 to n=50 (b), and the aperture from a=8 10^{-4} m to a=1.4 10^{-3} m (d).

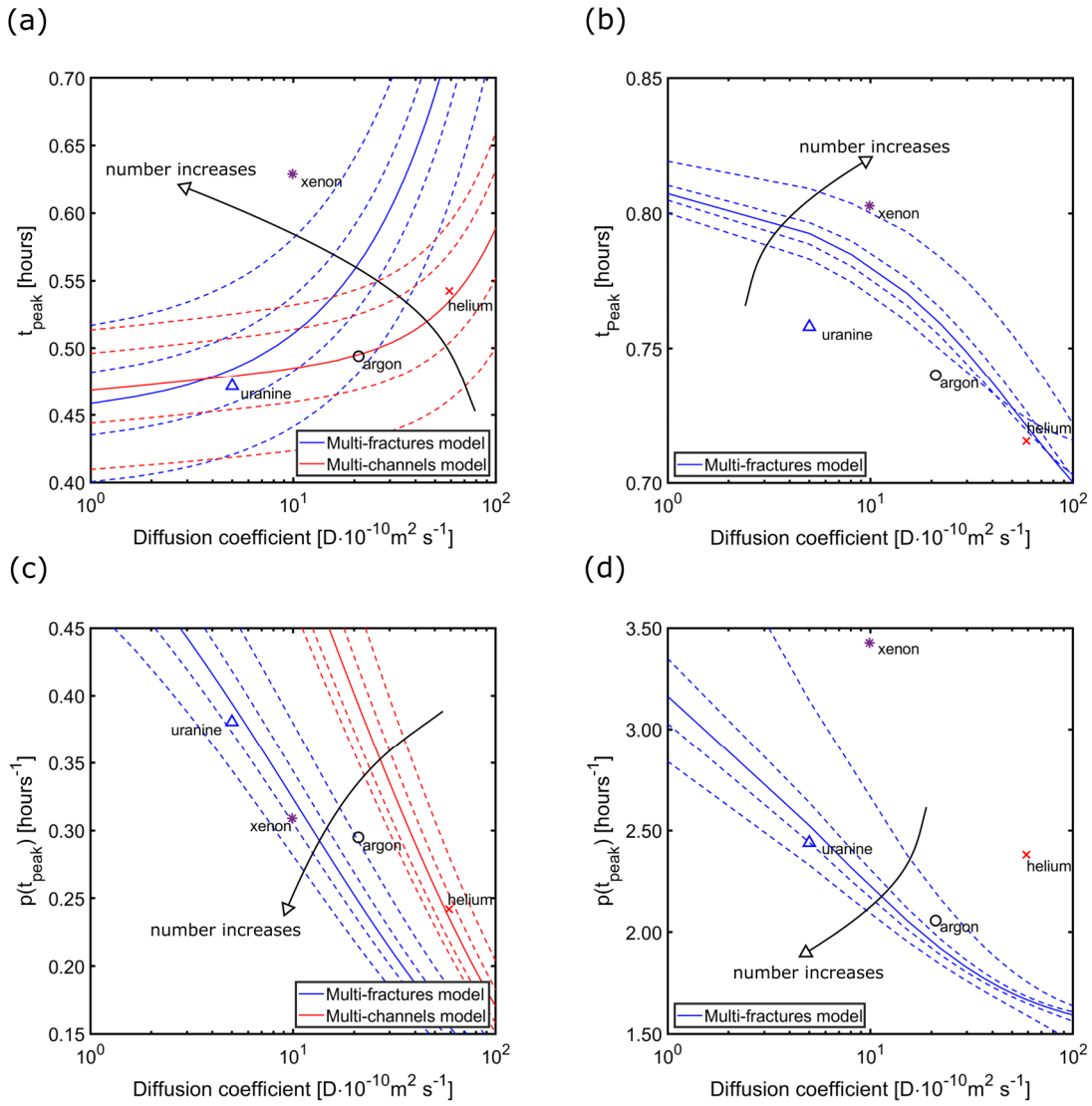

Figure S8. Sensitivity analysis of modelled peak time and peak amplitude when varying the number of fractures/channels for the convergent test peak time (a) and amplitude (c) and for the push-pull test peak time (b) and amplitude (d). In the convergent test, the number of fractures was varied from 35 to 45 and the number of channels from 600 to 750. In the push-pull case, the number of fractures was varied from 1 to 7 fractures.

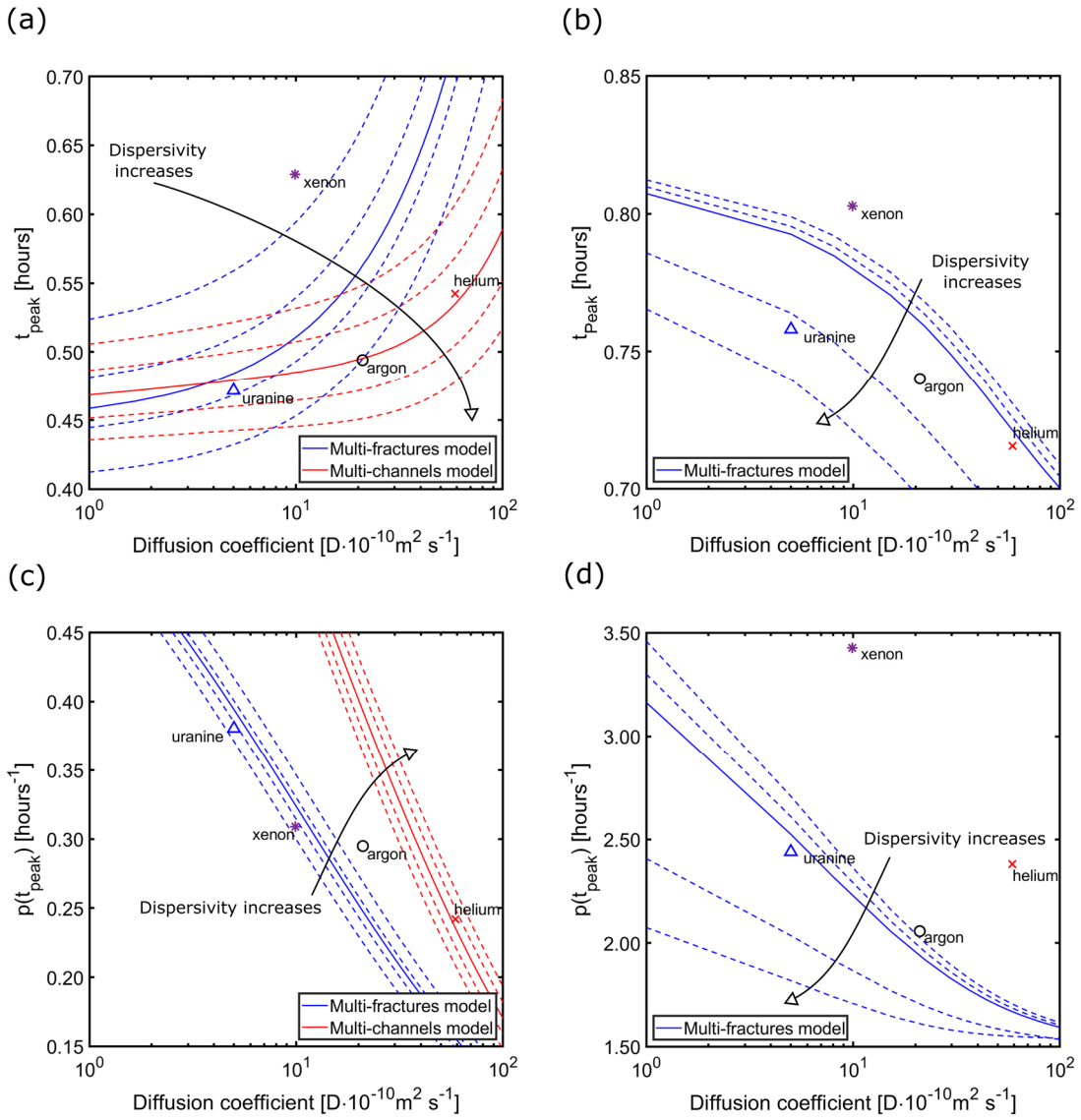

Figure S9. Sensitivity analysis of modelled peak time and peak amplitude on dispersivity for peak times of the convergent (a) and push-pull (b) test as well as for the peak amplitude for convergent (c) and push-pull (d) test. In the convergent test, the dispersivity was varied from 2 m to 2.75 m for uranine and from 1.3 m to 1.7 m for helium. In the push-pull case, the dispersivity was varied from 0.08 m to 0.3 m.

Text S4: Change of fracture-matrix interaction mode with diffusion coefficient

Figure S10 shows that the parallel plate model using the adjusted parameters from the uranine convergent test data fails to predict the helium data and vice versa. This mismatch of the model with data confirms the change of the dominant fracture-matrix exchange mode from one-dimensional (parallel plate model) to radial (channel model) with increasing diffusion coefficient as anticipated from the analysis of the breakthrough curve tailing.

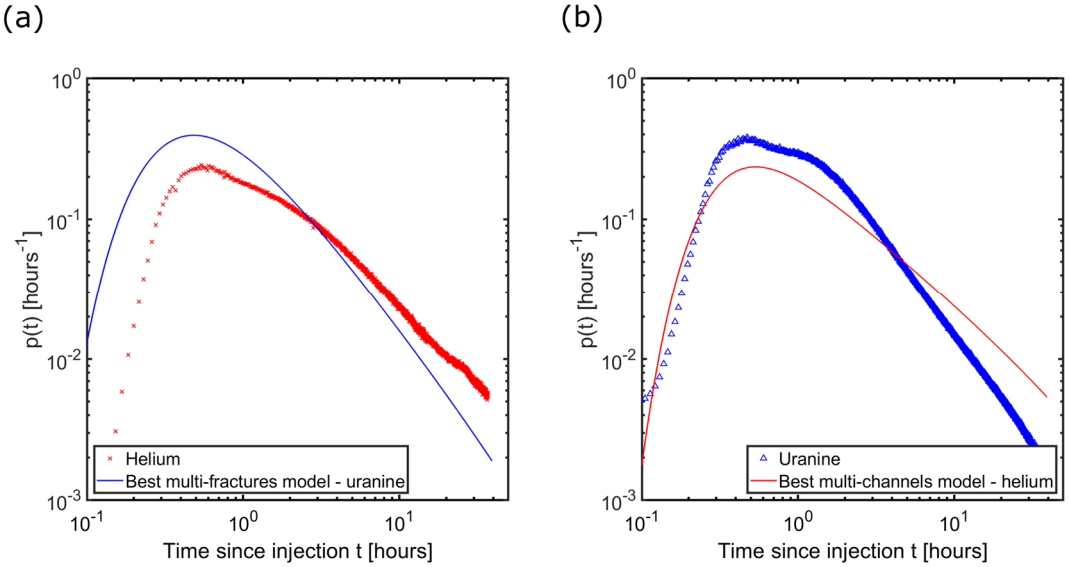

Figure S10. Prediction of (a) helium breakthrough using the parameters adjusted for the uranine breakthrough curve for the convergent test, and (b) uranine breakthrough using the parameters adjusted for the helium breakthrough curve for the convergent test.